Dual-doping NiMoO$_4$ with multi-channel structure enable urea-assisted energy-saving H$_2$ production at large current density in alkaline seawater

Lili Guo [a], Jingqi Chi [a,b,*], Jiawei Zhu [a,b], Tong Cui [a], Jianping Lai [a], Lei Wang [a,c,*]

[a] *Key Laboratory of Eco-chemical Engineering, Ministry of Education, International Science and Technology Cooperation Base of Eco-chemical Engineering and Green Manufacturing, College of Chemistry and Molecular Engineering, Qingdao University of Science and Technology, Qingdao 266042, PR China*
[b] *College of Chemical Engineering, Qingdao University of Science and Technology, Qingdao 266042, PR China*
[c] *College of Environment and Safety Engineering, Qingdao University of Science and Technology, Qingdao 266042, PR China*

ARTICLE INFO

ABSTRACT

Seawater electrolysis is an efficient method for producing carbon-neutral hydrogen; however, it is hindered by high energy cost and chlorine evolution reaction. In this study, we report Ru, P dual-doped NiMoO$_4$ multichannel nanorods in-situ grown on nickel foam (Ru/P-NiMoO$_4$ @NF), which can achieve chlorine-free hydrogen production by coupling seawater splitting with thermodynamically favorable urea oxidation. The Ru/P-NiMoO$_4$ @NF exhibits bifunctional activity with working potentials of 0.23 V to deliver 3000 mA cm^{-2} for HER and 1.46 V to deliver 1000 mA cm^{-2} for UOR. The overall urea splitting system in the two-electrode electrolyzer require low voltage of 1.73 V to drive 500 mA cm^{-2}, and demonstrate remarkable durability to keep above 100 mA cm^{-2} for 145 h. Density functional theory calculations reveal that dual-doping modulate the ᴅ-band center of catalyst, thus enhancing the adsorption of reactants and intermediates. This work provides information for designing catalysts for combing seawater splitting with urea purification.

1. Introduction

Hydrogen (H$_2$) as an energy carrier is a potential alternative to conventional fossil fuels due to its high energy density of 142 MJ kg^{-1} and zero emissions [1–3]. The hydrogen evolution reaction (HER) via electrochemical water splitting using renewable energy sources and alkaline electrolyzers can effectively minimize energy crises and environmental pollution [4–6]. Considering the less availability of pure water, the use of seawater as HER feedstock is a promising alternative. Thus, the use of free and abundantly available seawater as a feedstock for HER has attracted increasing attention [7–9]. However, conventional catalysts are usually ineffective for alkaline seawater electrolysis owing to their unstable nature [10–13]. Another reasons for the ineffectiveness of conventional catalysts are as follows: the chlorine evolution reaction (CER) at the anode may be competing with the oxygen evolution reaction (OER) for the direct alkaline seawater electrolysis because the thermodynamic potential of CER is only approximately 480 mV larger than that of OER [14–17], and the formation of corrosive hypochlorite may block and destroy the active sites of catalysts, causing

environmental hazards [18–21]. The CER can be prevented by restricting the overpotential ($<$ 0.48 V) under alkaline conditions; however, the electrolysis for HER cannot meet industrial standards (500–1000 mA cm^{-2}) [22–24]. The electrocatalytic oxidation of thermodynamically favorable small molecules to replace slow water oxidation provides a potential strategy for chlorine-free and energy-saving H$_2$ production [25–27]. The urea (CO(NH$_2$)$_2$) oxidation reaction (UOR) (CO(NH$_2$)$_2$ (l) + 6OH$^-$ → N$_2$ (g) + 5 H$_2$O (l) + CO$_2$ (g) + 6e$^-$, E^0 = 0.37 V vs. RHE) is more efficient for H$_2$ production than OER (1.23 V vs. RHE). Urea is an advanced hydrogen carrier with a hydrogen content of 6.67 wt%, which is a potentially free source from human urine and urea-rich wastewater [28–30]. However, UOR is characterized by sluggish kinetics because of the complex six-electron transfer process and multiple formation/desorption of intermediates [31–33]. Some studies have reported great progress in UOR-assisted H$_2$ production, such as Ni-Mo-based nanostructures and metallic Ni(OH)$_2$ nanosheets [26,34, 35]. Despite the progress recorded, several challenges, including production cost, still require attention. First, the development of bifunctional cathodic HER and anodic UOR catalysts with high activity will

decrease the cost of production, which remains challenging [36,37]. Second, the theoretical insight into the underlying mechanism for the HER and UOR process is essential for the development of electrochemistry [38,39].

In this study, we report a Ru/P dual-doped $NiMoO_4$ @NF (Ru/P-$NiMoO_4$ @NF) nanorods with a multichannel structure as the bifunctional HER and UOR electrocatalyst in alkaline seawater. The multichannel Ru/P-$NiMoO_4$ @NF is synthesized via ion exchange between Ru and Ni and followed by a low-temperature phosphorization. The multichannel Ru/P-$NiMoO_4$ @NF can expose more electrochemical surface active areas for seawater electrolysis. The optimized multichannel Ru/P-$NiMoO_4$ @NF nanorods achieve large current densities of 3000 mA cm^{-2} at 0.23 V for HER, 1000 mA cm^{-2} at 1.46 V for UOR, and chlorine-free H_2 production at a large current density. The overall urea splitting (OUS) system in the two-electrode system requires an ultralow cell voltage of 1.73 V to deliver 500 mA cm^{-2} for 145 h, demonstrating remarkable durability. In-depth DFT studies show that Ru/P doping can modulate the D-band center, which can simultaneously facilitate the absorption of reactants. This work presents a strategy for developing a highly active doped electrocatalyst for energy-saving hydrogen production and urea purification-based hybrid seawater splitting.

2. Experimental section

2.1. Chemical and materials

Nickel nitrate hexahydrate (Ni(NO$_3$)$_2$0.6 H$_2$O), sodium molybdate dehydrate (Na$_2$MoO$_4$0.2 H$_2$O), ruthenium chloride (RuCl$_3$), sodium hypophosphite (NaH$_2$PO$_2$·H$_2$O(NaPO$_2$H$_2$)) were purchased from Aladdin Industrial Corporation. The seawater is taken from Shilaoren Bathing Beach in Qingdao, Shandong Province, and used after suction filtration.

2.2. Materials synthesis

2.2.1. Synthesis of NiMoO$_4$ @NF precursor

$NiMoO_4$ @NF precursor was in-situ grown on the surface of NF via a facile hydrothermal approach. Nickel foam (NF) (1 cm × 2 cm) was first immersed and then sonicated in 0.1 M H$_2$SO$_4$, acetone solution, and ethanol solution for 20 min to remove the oxide layer on the surface, then the cleaned NF were dried in a vacuum oven. Then, the same mole ratio of Ni(NO$_3$)$_2$0.6 H$_2$O and Na$_2$MoO$_4$0.2 H$_2$O were dissolved in 30 ml deionized water under stirring until completely dissolved. Afterward, the dried NF were subsequently immersed into the above solution, and then were transferred into 50 ml of Teflon-lined stainless autoclave and heated at 160 °C for 6 h. After cooling down, the as-obtained sample were taken out and washed with ethanol and DI water for several times, and the $NiMoO_4$ @NF precursor were obtained after drying.

2.2.2. Synthesis of Ru-NiMoO$_4$ @NF

The above prepared $NiMoO_4$ @NF precursor was immersed in 0.005 g ml^{-1} of RuCl$_3$ aqueous solution for 6 h, and then dried to obtain Ru-$NiMoO_4$ @NF.

2.2.3. Synthesis of Ru/P-NiMoO$_4$ @NF

For the synthesis of Ru/P-$NiMoO_4$ @NF, Ru-$NiMoO_4$ @NF and 0.5 g of NaH$_2$PO$_2$ were placed in a porcelain boat and annealed at 350 ℃ for 2 h in Ar atmosphere with the heating rate of 2 ℃ min^{-1}. Then, Ru/P-$NiMoO_4$ @NF was obtained after natural cooling. To investigate the effect of the Ru loading amount on the activity of the catalyst, the concentration of RuCl$_3$ was controlled to prepare series Ru/P-$NiMoO_4$ @NF catalysts with different Ru loadings. Specifically, Ru aqueous solutions with concentrations of 0, 0.005 and 0.01 g ml^{-1} were used. For comparison, P-$NiMoO_4$ @NF was prepared by replacing the Ru-$NiMoO_4$ @NF with $NiMoO_4$ @NF, and all other synthesis methods were the same with that of Ru/P-$NiMoO_4$ @NF.

2.3. Materials characterization

The morphology of the catalysts was characterized by scanning electron microscopy (SEM) with an accelerating voltage of 10 kV. The microstructure and morphology of the catalysts were observed by Transmission electron microcopy (TEM) on a JEM-F200. The spatial distribution of elements were characterized by TEM elemental mappings on a JEM-F200. X-ray diffraction (XRD) analysis was recorded on X′Pert PRO MPD in the 2θ ranging from 5 to 90° with a scanning rate of 1° min^{-1}. The superficial chemical states were characterized by X-ray photoelectron spectroscopy (XPS) measurements on the AXIS SUPRA (Al Kα source, 15 mA and 14 kV). Raman spectroscopy was performed on Renishaw in Via Raman microscope under the excitation laser of 532 nm.

2.4. Electrochemical measurements

Electrochemical tests were performed with a three-electrode system by a Gamry Reference 3000. Saturated calomel electrode was employed as reference electrode, the graphite rod was used as counter electrode, and the as-prepared 1 cm × 1 cm samples were directly used as working electrode. All of the potentials involved were based on the reversible hydrogen electrode (RHE): $E_{RHE} = E_{SCE} + 0.059$ pH + 0.243. The electrochemical properties evaluation of all prepared electrodes were performed in 1.0 M KOH, 1.0 M KOH+ 0.5 M NaCl, 1.0 M KOH+seawater, and 1.0 M KOH+seawater+ 0.5 M urea for HER, OER, and UOR characterization with iR compensation at a scan rate of 5 mV s^{-1}. EIS measurements were carried out in the frequency range from 0.1 Hz to 100 kHz with an amplitude of 5 mV. The stability of Ru/P-$NiMoO_4$ @NF in different solutions was tested by chronoamperometric i-t measurement.

2.5. Computational details

The present first principle DFT calculations was performed by Vienna Ab initio Simulation Package (VASP) with the projector augmented wave (PAW) method [40,41]. The exchange functional is processed using the generalized gradient approximation (GGA) of the Perdew-Burke-Emzerhof (PBE) functional [42]. The energy cutoff for the plane-wave basis expansion was set to 450 eV, and the convergence criterion for the geometric relaxation was set to force less than 0.03 eV/Å per atom. Dispersive interactions were described using Grimme's DFT-D3 method [43]. Partial occupancies of the Kohn−Sham orbitals were allowed using the Gaussian smearing method with a width of 0.05 eV. Throughout the calculations, the Brijulin area was sampled with a Monkhorst grid of 2 × 2 × 1. A convergence energy threshold of 10^{-5} eV was applied from the coherent calculations. To avoid interaction between two adjacent images, a 15 Å vacuum space along the z direction was added.

3. Results and discussion

3.1. Synthesis and characterization of multi-channel Ru/P-NiMoO$_4$@NF nanorods

Fig. 1a shows a schematic diagram of the synthetic scheme of the multichannel Ru/P-$NiMoO_4$ @NF hollow nanorods, where commercial nickel foam with a smooth surface was used as conductive support due to its excellent electrical conductivity and high surface area (Fig. S1). First, we synthesized solid $NiMoO_4$ nanorod arrays on NF via a hydrothermal method, and the synthesized solid $NiMoO_4$ nanorod arrays were immersed in Ru aqueous solution to obtain multichannel hollow Ru-$NiMoO_4$ @NF nanorods. Finally, the multichannel hollow Ru/P dual-doped $NiMoO_4$ @NF nanorods were obtained via thermal phosphorization reaction. Figs. 1b–e, S2, and S3 display the typical morphology and structure of the catalysts at different stages. First, as shown, a large number of solid $NiMoO_4$ nanorods with smooth surfaces are uniformly
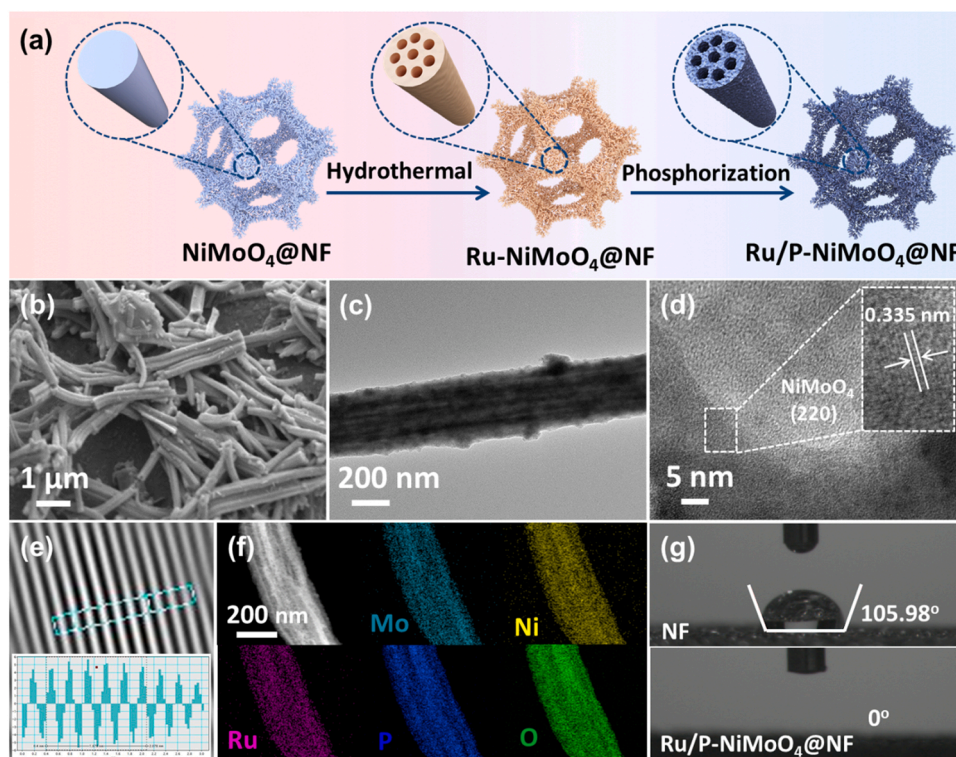
Fig. 1. (a) Schematic illustration of the formation process of Ru/P-NiMoO₄ @NF. (b) SEM, (c) TEM, (d) HRTEM and (e) the corresponding FFT images of Ru/P-NiMoO₄ @NF. (f) TEM image and corresponding elemental mappings of Ru/P-NiMoO₄ @NF. (g) Static water droplets contact angle at NF and Ru/P-NiMoO₄ @NF.

and vertically grown on the NF through the hydrothermal reaction of $Na_2MoO_4 0.2\ H_2O$ and $Ni(NO_3)_2 0.6\ H_2O$; the diameter of NiMoO₄ nanorod is ~400–600 nm (Fig. S2a and b). After the NiMoO₄ nanorod was immersed in Ru aqueous solution, an intact nanorod-like structure of NiMoO₄ nanorod is still preserved. However, the surface of the NiMoO₄ nanorod become rough, and a strange multichannel hollow structure appear in the Ru-NiMoO₄ @NF nanorods (Fig. S3a and b), which may be attributed to the partial Ni species in NiMoO₄ corroded to soluble Ni ions with the addition of Ru^{3+}. After the thermal phosphorization process, the obtained Ru/P-NiMoO₄ @NF still shows a well-distributed multichannel hollow structure with a rough surface, and the surface of every nanorod is covered with numerous nanoparticles (Figs. 1b, c, and S4). As shown in Fig. 1d and e, the high-resolution transmission electron microscopy (HRTEM) and the corresponding fast fourier transform (FFT) images of Ru/P-NiMoO₄ @NF exhibit clear lattice fringes in the whole vision, and the lattice fringe with an interplanar spacing of 0.335 nm is assigned to the (220) plane of NiMoO₄, demonstrating the composition of Ru/P-NiMoO₄ @NF hollow nanorods. Energy-dispersive X-ray spectroscopy mapping analysis (Figs. 1f and S5) further confirm the typical hollow nanorod structure, which clearly show the uniform distribution of Mo, Ni, Ru, P, and O in the entire hollow nanorod. Moreover, the surface atomic percentages of Mo, Ni, Ru, P, and O are 6.65 %, 26.53 %, 2.88 %, 15.36 %, and 45.68 %, respectively (Fig. S5), and the content of the noble metal is less than that of commercial Pt/C. For comparison, we also investigated the morphology change of Ru/P-NiMoO₄ @NF with different Ru loadings by adjusting the concentration of Ru aqueous solution. Figs. S6, 1b, and S7 show scanning electron microscopy (SEM) images of Ru/P-NiMoO₄ @NF series samples. The results show that the structure of nanorods aggregate together with the increasing Ru content. The optimal Ru concentration was determined to be 0.005 g ml^{-1}, and this concentration was used for subsequent analyses unless otherwise specified. Moreover, wettability studies reveal that the pure NF is hydrophobic with a contact angle of 105.98° (Fig. 1g), while the prepared Ru/P-NiMoO₄ @NF displays a super hydrophilic surface that can strengthen

the electrolyte affinity and permeation hydrophilic, which accelerate the water splitting process of the Ru/P-NiMoO₄ @NF [44].

The crystal structure and chemical state of the prepared materials were examined via X-ray powder diffraction (XRD) and X-ray photoelectron spectroscopy (XPS). As displayed in Figs. 2a and S8, the diffraction peaks of the Ru/P-NiMoO₄ @NF sample scratched from the Ni foam surface (Fig. 2a) confirms the existence of the NiMoO₄ phase (PDF No. 45-0142), consistent with that of the NiMoO₄ @NF precursor. By comparing the XRD patterns of the Ru/P-NiMoO₄ @NF sample with different Ru concentrations, no new substances appear except NiMoO₄ and Ni substrate, revealing the doping of Ru and P into the NiMoO₄ structure without forming new phases. The Raman spectrum in Fig. 2b further confirms the formation of NiMoO₄, where the vibrations of Ni-O, Mo-O and Mo-O-Mo are observed at 372, 353 and 265 cm^{-1}, respectively, and three active oscillators at 827, 870, and 946 cm^{-1} are related to the Mo-O-Ni tensile mode, confirming the existence of NiMoO₄ phase [45,46]. XPS survey spectra (Fig. S9) confirms the coexistence of Mo, Ni, Ru, P, and O in the Ru/P-NiMoO₄ @NF. Compared with the P-NiMoO₄ @NF precursor, the peaks of the Ru/P-NiMoO₄ @NF are diffused with concomitant angular shifts, which can be reasonably attributed to partial Ru doping into the lattice of NiMoO₄. The fitted curve of the Mo 3d spectrum shown in Fig. 2c is deconvoluted into Mo^0 (229.3 and 231.2 eV), Mo^{4+} (230.1 and 233.3 eV), and Mo^{6+} (232.3 and 235.4 eV) [45]. The Ni 2p spectrum of Ru/P-NiMoO₄ @NF in Fig. 2d shows that five peaks are deconvoluted at 851.7, 856.2, 862.1, 874.1, and 880.7 eV [46,47]. The peaks of Ni $2p_{3/2}$ at 852.7 eV can beassigned to metallic Ni [48,49]. The peaks at 856.2 and 874.1 eV can be ascribed to Ni^{2+}. The relative satellite peaks at 862.1 and 880.7 eV may originate from the surface oxidation of the catalyst [50,51]. Furthermore, the binding energy of Ni in Ru/P-NiMoO₄ @NF shifts towards lower energy compared with P-NiMoO₄ @NF, implying an electron effect between Ru and Ni. For the spectrum of P 2p (Fig. 2e), the peak at 133.8 eV corresponds to P-O species likely from surface oxidation or phosphorization process [52,53]. Fig. 2f shows the high-resolution spectrum of Ru 3p of the Ru/P-NiMoO₄ @NF, where two strong peaks at 461.7 and 483.7 eV are
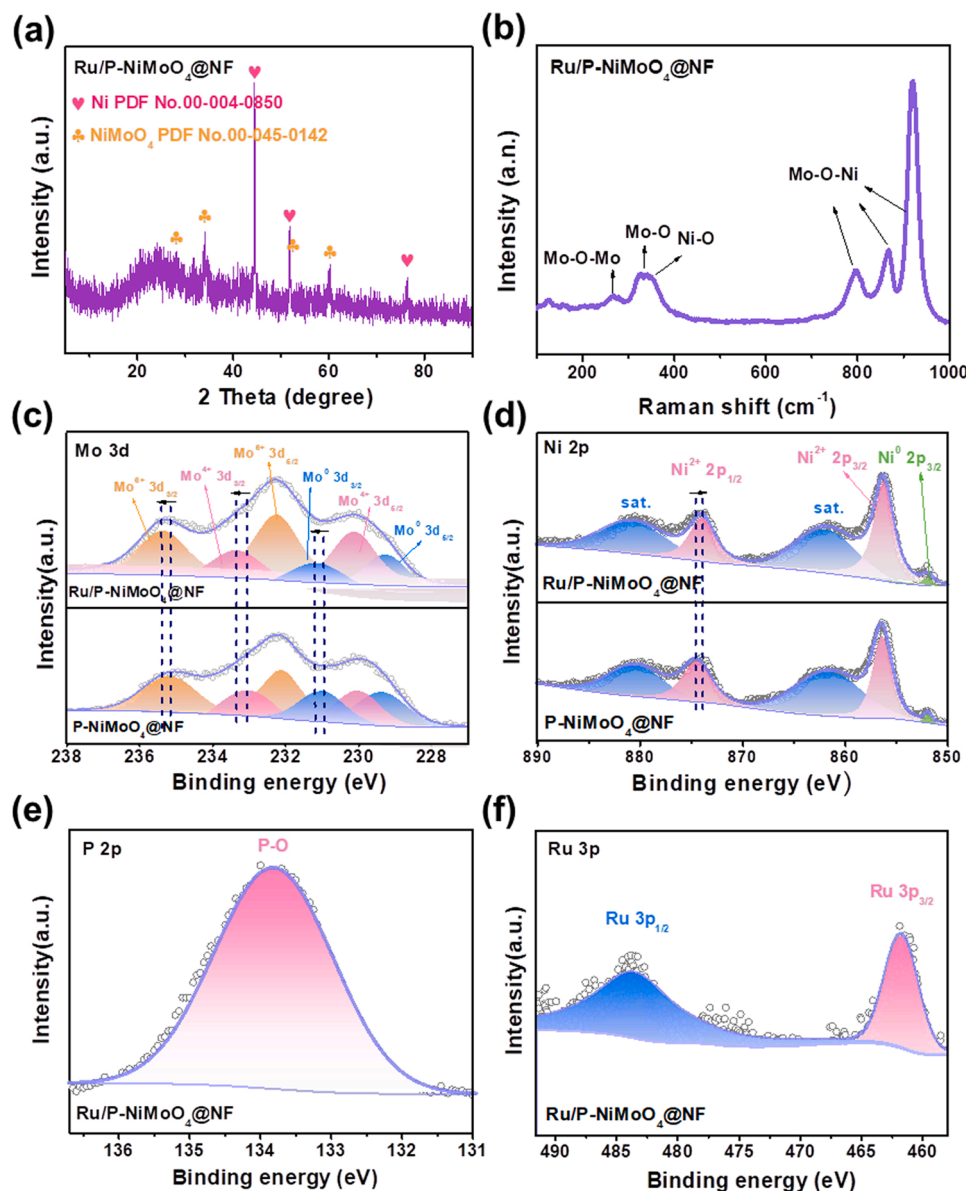
Fig. 2. (a) XRD patterns of Ru/P-NiMoO$_4$ @NF. (b) Raman spectrum of Ru/P-NiMoO$_4$ @NF. (c) Mo 3d and (d) Ni 2p spectra of Ru/P-NiMoO$_4$ @NF and P-NiMoO$_4$ @NF. (e) P 2p and (f) Ru 3p spectra of Ru/P-NiMoO$_4$ @NF.

assigned to Ru $3p_{3/2}$ and $3p_{1/2}$ of Ru^0 [54,55]. The above results demonstrate the synthesis of the NiMoO$_4$ structure and effective doping of P and Ru into the NiMoO$_4$ structure.

3.2. Oxygen and hydrogen evolution catalysis

We investigated the HER and OER activities of the prepared Ru/P-NiMoO$_4$ @NF and comparative catalysts in 1.0 M KOH. The catalysts were compared with benchmark commercial Pt/C (HER) and RuO$_2$ (OER) catalysts. As shown by the LSV curve results in Fig. 3a, the prepared multichannel Ru/P-NiMoO$_4$ @NF catalyst exhibits excellent bifunctional activity for both HER and OER. The LSV curves show the overpotentials as low as 232 and 423 mV can achieve large current densities of − 3000 and 1000 mA cm^{-2}, respectively, much smaller than those of P-NiMoO$_4$ @NF (519 and 566 mV), NiMoO$_4$ @NF (456 and 525 mV), the benchmark Pt/C and RuO$_2$ electrode (430 and 719 mV), and NF (530 and 719 mV) (Fig. 3b). The result also reveals that Ru and P dual-doping enhance both HER and OER performance. Compared with transition metal-based bifunctional electrocatalysts reported in recent

years, multichannel hollow Ru/P-NiMoO$_4$ @NF nanorod exhibited excellent HER/OER activity in alkaline media (Fig. 3c, Table S1). In addition, the Tafel slopes for Ru/P-NiMoO$_4$ @NF catalyst are calculated to be 50.1 and 160.6 mV dec^{-1} in HER and OER, respectively, indicating the rapid HER and OER reaction kinetics of the Ru/P-NiMoO$_4$ @NF electrode (Figs. S10a and S11a). Moreover, the Ru/P-NiMoO$_4$ @NF electrode exhibits a smaller semicircle and a lower charge transfer resistance (R_{ct}) value in the low-frequency range than those of the control samples, according to electrochemical impedance spectroscopy (EIS) measurement, indicating rapid charge transfer within the Ru/P-NiMoO$_4$ @NF catalyst (Figs. S10b and S11b) [56]. In addition, the HER and OER activities of other Ru/P-NiMoO$_4$ @NF catalysts with different Ru loadings were investigated (Figs. S12–S13), and the catalyst prepared with the Ru concentration of 0.005 g ml^{-1} exhibits the best HER and OER activities.

Then, we investigated the HER and OER activities of Ru/P-NiMoO$_4$ @NF in different alkaline solutions. As shown in Fig. 3d, the multichannel hollow Ru/P-NiMoO$_4$ @NF catalyst exhibits excellent HER catalytic activity in an alkaline-simulated seawater solution (1.0 M
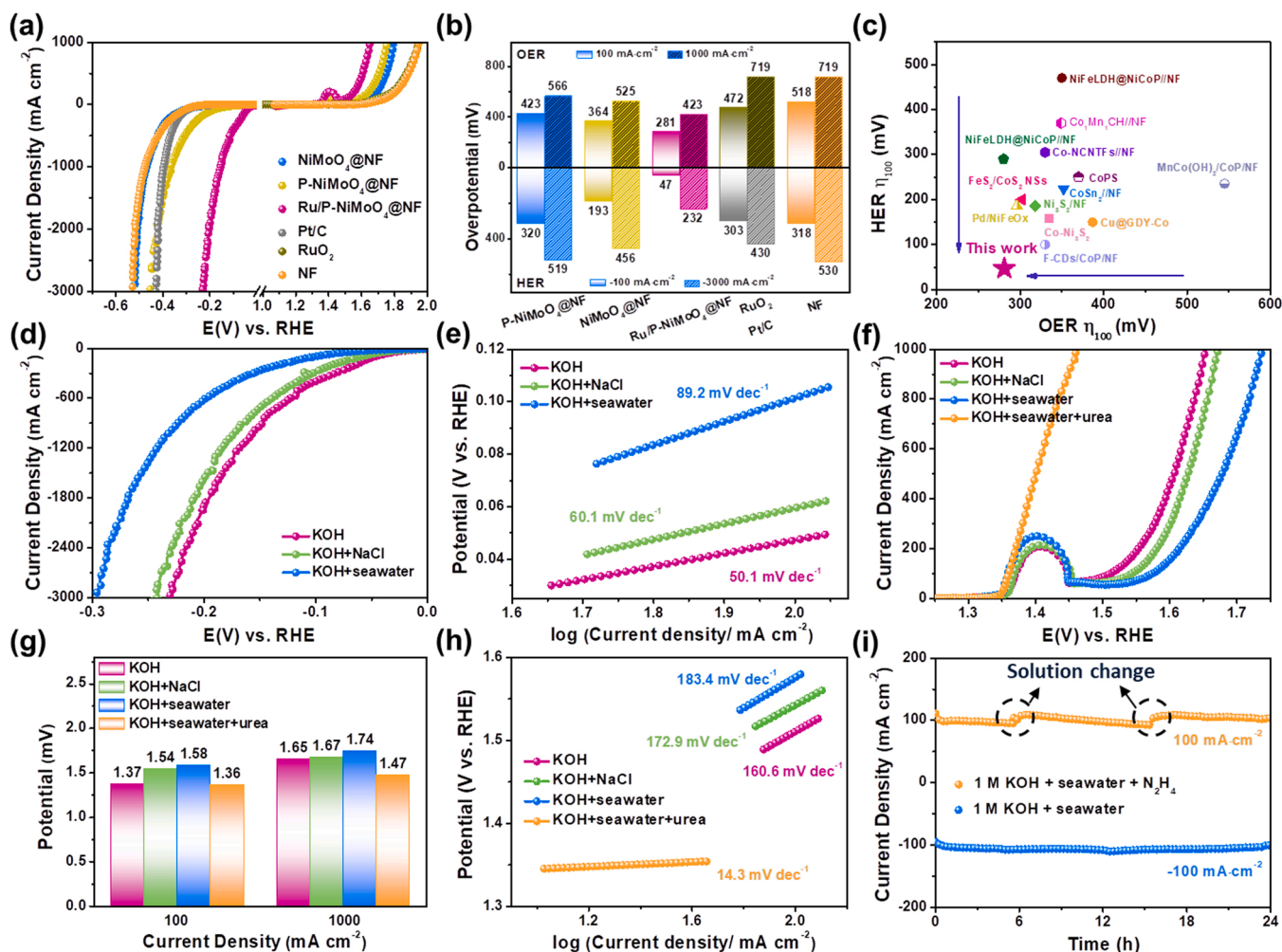
Fig. 3. HER and OER performance of the as-prepared catalysts for (a) Polarization curves, (b) overpotentials at different current densities, (c) comparison of the overpotentials with other reported bifunctional electrocatalysts in 1.0 M KOH at 100 mA cm^{-2}. (d) Polarization curves and (e) corresponding Tafel plots for HER in different solutions. (f) Polarization curves, (g) potentials at 100 and 1000 mA cm^{-2} in different solutions, and (h) corresponding Tafel plots for OER and UOR. (i) Chronoamperometry i-t curve of 24 h for HER and UOR.

KOH+0.5 M NaCl). The ultra-large current densities of 1000 and 3000 mA cm^{-2} are achieved with the overpotential of 173 and 242 mV, respectively (Fig. S14). This performance is extremely close to that in 1.0 M KOH electrolyte, indicating selectivity for HER in saline conditioned by an alkaline system. We also explore the HER performance in an alkaline natural seawater electrolyte (1.0 M KOH+seawater). The natural seawater is collected from Shilaoren Beach, Qingdao, Shandong. The electrochemical results show that the HER activity of the Ru/P-NiMoO$_4$ @NF catalyst is slightly attenuated compared with the other two electrolytes, but can still achieve 3000 mA cm^{-2} with the low overpotential of only 299 mV) and Tafel slope (89.2 mV dec^{-1}) is still achieved (Fig. 3e). The slight activity decay may be attributed to some insoluble precipitates [e.g., Mg(OH)$_2$ and Ca(OH)$_2$] covering the surface active sites of the electrode [7]. Likewise, the multichannel hollow Ru/P-NiMoO$_4$ @NF catalyst also exhibit outstanding OER activity in alkaline simulation and natural seawater electrolyte (Fig. 3f). However, the onset potential of CER is approximately 490 mV larger than that of OER. The UOR provides the extra potential to prevent the occurrence of CER without restricting the current and H$_2$ yielding efficiency during the electrolysis process. Therefore, the UOR polarization curve of the Ru/P-NiMoO$_4$ @NF catalyst was presented to compare its OER activities in alkaline seawater solution (1.0 M KOH+seawater+0.5 M urea) (Fig. 3f). The LSV results show that the Ru/P-NiMoO$_4$ @NF catalyst exhibit excellent UOR performance with the working potential of 1.46 V

to produce a large current density of 1000 mA cm^{-2}, which is 270 mV lower than that of OER in alkaline seawater solution (Fig. 3g). Moreover, as shown in Fig. 3h, the Ru/P-NiMoO$_4$ @NF exhibited extremely low Tafel slope of 14.3 mV dec^{-1} for UOR process. This showed that the UOR exhibited more favorable catalytic kinetics than OER. In addition, the UOR performance of the different prepared catalysts is compared, and the results show that the Ru/P-NiMoO$_4$ @NF exhibits excellent performance for UOR (Fig. S15). Stability is a crucial parameter to evaluate the excellent performance of catalysts in electrochemical reactions. As shown in Fig. 3i, during a long-term test (up to 24 h), the Ru/P-NiMoO$_4$ @NF exhibits excellent stability with a slight change in current density at a constant overpotential for HER and UOR catalysis in seawater. Furthermore, the SEM and TEM images after the stability test demonstrate strong supportability and high integrity of the multichannel nanorod-like structure of the Ru/P-NiMoO$_4$ @NF catalyst, which is favorable for the rapid release of gaseous products (Figs. S16–S18). The high-resolution XPS analysis (Fig. S19) indicates the existence of Mo and Ni after HER and OER stability. The negative shift of Mo and Ni after the HER reaction imply the partial reduction of Mo and Ni during the HER process, and the slight changed in signals of Mo and Ni after the OER test confirm the stable property of the Ru/P-NiMoO$_4$ @NF structure [57].

3.3. Overall urea splitting (OUS) in seawater

Based on the excellent HER and UOR catalytic performance of the Ru/P-NiMoO$_4$ @NF catalyst, we used the Ru/P-NiMoO$_4$ @NF electrode as anode and cathode to construct a two-electrode alkaline seawater electrolyzer, and the OUS performance was investigated. Commercial Pt/C||RuO$_2$ performances were compared. First, we compared the LSV curves of the Ru/P-NiMoO$_4$ @NF couple for two-electrode electrolysis in different solutions. Fig. 4a compares LSV curves of OUS and overall seawater splitting (OWS). The comparison results show that the UOR-assisted seawater splitting effectively improve the hydrogen production efficiency. Specifically, the Ru/P-NiMoO$_4$ @NF couple could provide 500 mA cm^{-2} with an ultralow cell voltage of 1.73 V for OUS, which is 0.17 V lower than that for OWS in seawater, indicating that the UOR enhance the efficiency of the two-electrode electrolysis. In addition, the Ru/P-NiMoO$_4$ @NF couple exhibit a small Tafel slope of 133.2 mV dec^{-1} for OUS, indicating rapid reaction kinetics (Fig. 4b). The OUS performance rate of Ru/P-NiMoO$_4$ @NF is also higher than that of commercial Pt/C//RuO$_2$ couple in the urea-assisted seawater splitting system (Fig. S20). Such excellent catalytic OUS performance rate of the Ru/P-NiMoO$_4$ @NF is higher than most of the recently reported bifunctional non-precious metal catalysts in alkaline pure water electrolyte (Fig. 4c and Table S2). Fig. 4d demonstrates the excellent long-

term stability of the Ru/P-NiMoO$_4$ @NF couple for at least 145 h to keep the current density above 100 mA cm^{-2} for OUS in seawater electrolysis, as revealed by the chronoamperometry i-t test. By comparing the electricity expense in seawater electrolyzers, it can be found that using Ru/P-NiMoO$_4$ @NF as bifunctional electrocatalyst is superior to many recently reported works in terms of energy efficiency for hydrogen production (Figs. 4e , S21 and Table S3) [58]. In addition, the OUS process of the Ru/P-NiMoO$_4$ @NF couple can also be powered by solar panels. By comparing the volume sizes of initial and final balloons in different solutions at the same time, we observe that the amount of gas collected by the balloon for OUS is larger than that of OWS in seawater (Figs. 4f and S22). This result shows that energy-efficient hydrogen production can be achieved with the assistance of UOR. Figs. S23–S24 show that the hydrogen evolution rate of Ru/P-NiMoO$_4$ @NF is 1.7 mmol/h in 1 M KOH+seawater+ 0.5 M urea by the drainage method. The HSE-coupled UOR can alleviate the overall cell voltage of the HSE and purify the toxic urea in wastewater without using additional oxidants or complicated separation techniques. As shown in Fig. 4g, the urea with the concentration of 300 mg/L can be degraded to within 100 mg/L below 4 h at a current density of 150 mA cm^{-2}. Therefore, UOR-assisted water splitting is highly effective in practical applications. Using urea wastewater as an anolyte and cost-free seawater as a catholyte feed can effectively reduce the costs of
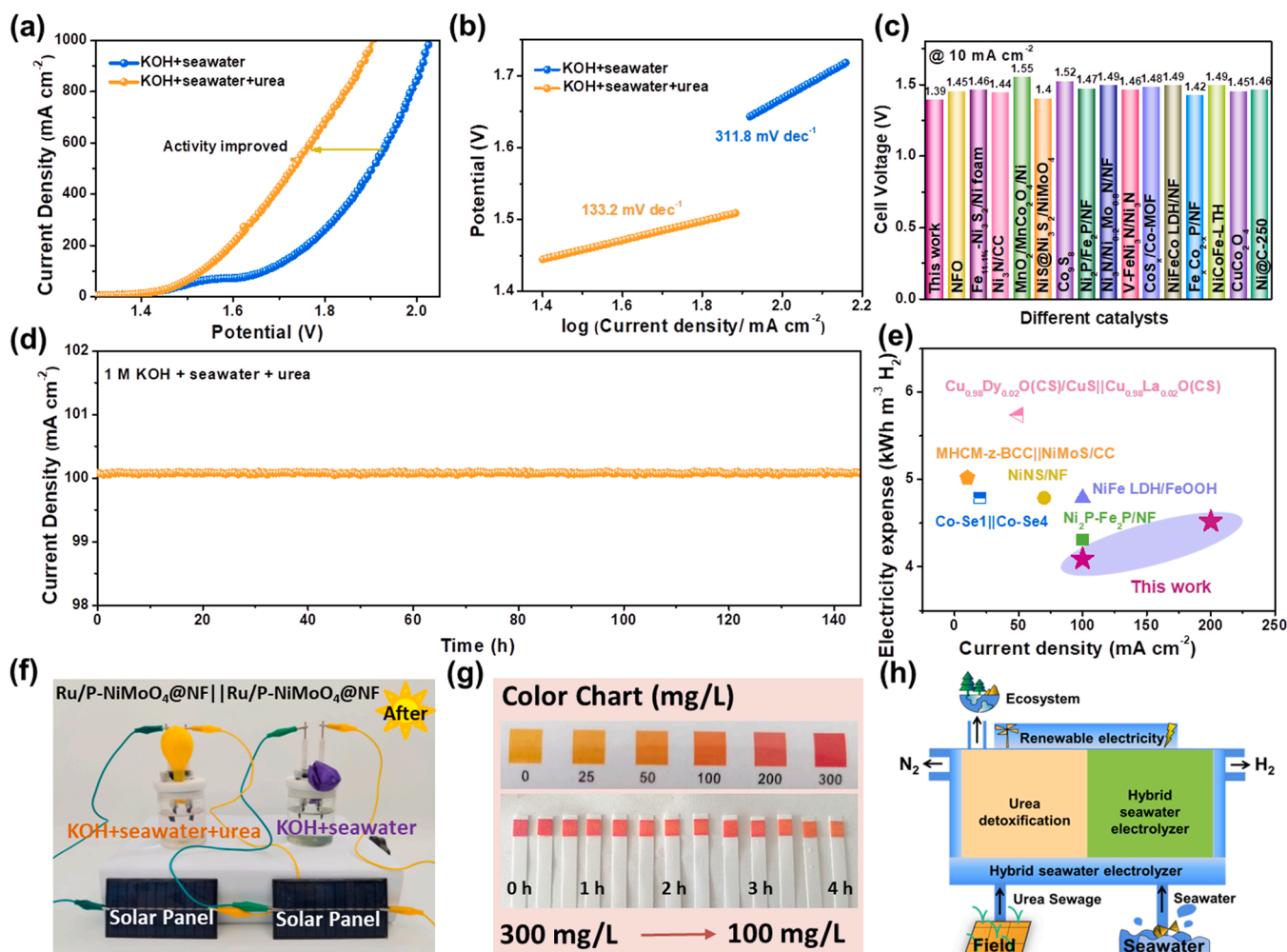
Fig. 4. (a) LSV curves and (b) corresponding Tafel plots of the Ru/P-NiMoO$_4$ @NF= | Ru/P-NiMoO$_4$ @NF for OWS and OUS in seawater. (c) Comparison of the overpotentials of the prepared Ru/P-NiMoO$_4$ @NF for OUS (at 10 mA cm^{-2}) with other reported bifunctional electrocatalysts. (d) Chronoamperometry i-t curve of the Ru/P-NiMoO$_4$ @NF couple for OUS. (e) Comparison of electricity expense with the state-of-the-art seawater electrolyzers. (f) Image of the electrocatalytic powered by the solar panels. (g) The color chart for the concentration degradation of urea at 150 mA cm^{-2}. (h) Schematic illustration of cost-effective and sustainable hydrogen production powered by renewables-powered HSE with seawater and industrial urea sewage as the feeds.

hydrogen generation. Thus, cost-effective and sustainable green hydrogen production can be achieved by transporting cost-free seawater and urea sewage into renewable energy-powered hybrid seawater electrolyzer (HSE) under strong solar radiation and wind (Fig. 4h).

3.4. Theoretical investigation of Ru/P-NiMoO₄ catalyst

The density functional theory (DFT) calculation was performed to understand the effect of the electronic structures of the Ru/P-NiMoO₄ system on HER and UOR performance at atomic insight. Combining the experimental result with the structural stability after doping based on calculation, the Ru and P dual-doped NiMoO₄ model is developed, where Ni and O atoms in NiMoO₄ are replaced with Ru and P atoms, respectively (Figs. 5a and S23). Fig. S26 shows that the formation energy of Ru replacing Ni atoms is 2.54 eV, and the formation energy of Ru replacing Mo atoms is 3.17 eV, indicating that Ru atoms are easier to replace Ni atoms. Fig. S27 shows the model diagram of Mo, Ni and Ru elements in Ru/P-NiMoO4 @NF as active sites to adsorb water molecules and urea molecules, respectively. Fig. S28 shows that the adsorption energies of H₂O and urea on Ru sites are lower than those of

Mo sites and Ni sites, which indicates that in the initial stage of the reaction, water and urea molecules will preferentially adsorb on Ru sites. The larger the adsorption energy are, the easier the activation and dissociation of H₂O and urea are, which is beneficial to the subsequent HER and UOR. Bader charge analysis is used to calculate the charge redistribution at the Ru/P-NiMoO₄ interface (Figs. 5b and S29). The co-doping of Ru and P decreases lost electrons in the Ru site of the Ru-NiMoO₄ from 1.248 to 0.909 after the formation of Ru/P-NiMoO₄, indicating that the co-doping of Ru and P increased electrons of the Ru site. The Ru sites with more electrons easily activate the reactants and enhance the adsorption of reaction intermediates, enhancing the electrocatalytic reaction. The three-dimensional charge density difference analysis (Fig. 5c) and ELF (Fig. 5d) reveal the electron localization behavior of Ru and P dopants. The analysis result shows that Ru dopants bond with P and O and the Ru-O coordination environment is changed, confirming that more charges participated in the subsequent electrochemical reaction [59]. The two-dimensional charge density difference analysis shows the accumulation (red) and depletion (blue) of charges more intuitively (Fig. S30) [60]. The work function was used to further study electron migration (Figs. 5e and S31). The result shows that the
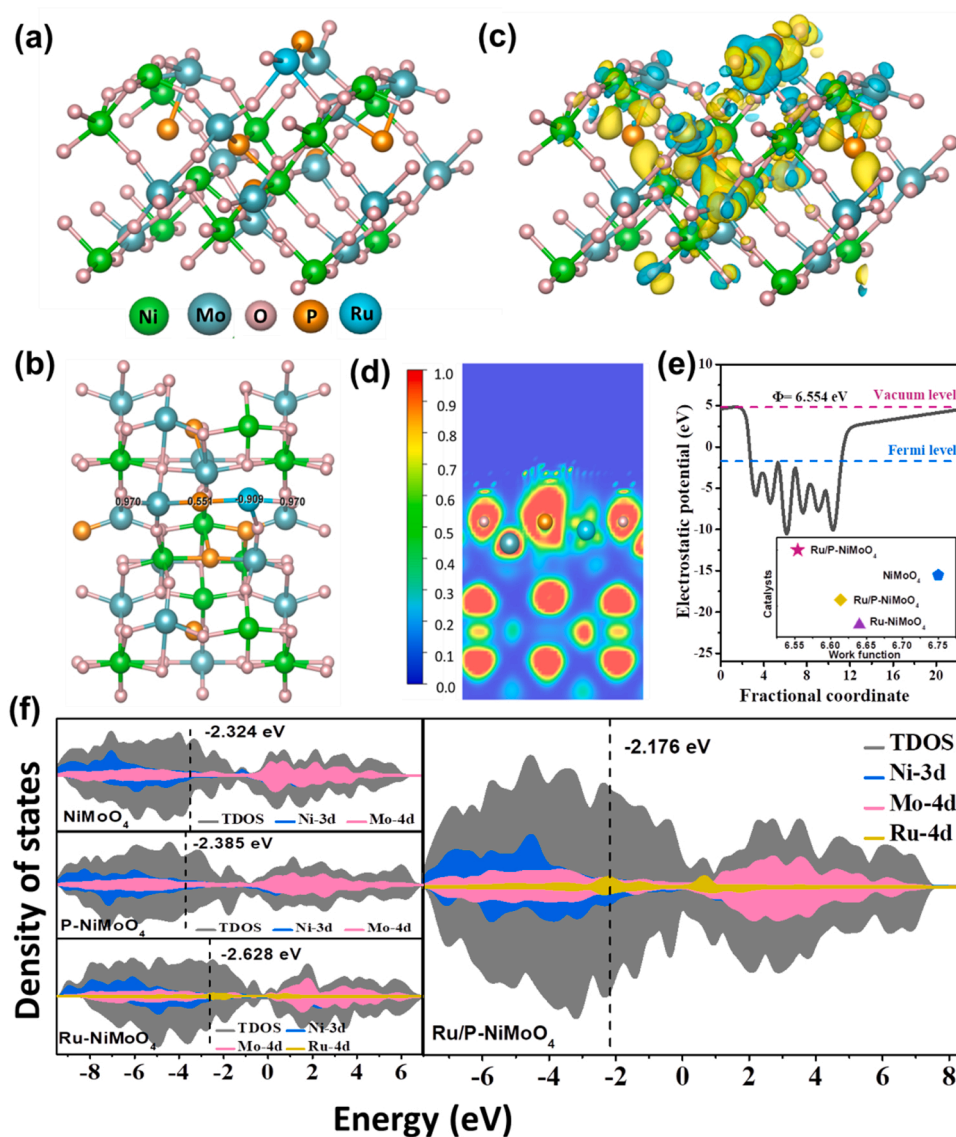
Fig. 5. (a) The atomic structure model of Ru/P-NiMoO₄. (b) Bader charge of Ru/P-NiMoO₄. (c) The three-dimensional charge density of Ru/P-NiMoO₄. (d) ELF of (220) surface of Ru/P-NiMoO₄. (e) The computed work functions of Ru/P-NiMoO₄. (f) Total and projected DOS for NiMoO₄, P-NiMoO₄, Ru-NiMoO₄, and Ru/P-NiMoO₄.

work function of Ru/P-NiMoO$_4$ at 6.554 eV is lower than that of NiMoO$_4$ (6.750 eV), P-NiMoO$_4$ (6.614 eV), and Ru-NiMoO$_4$ (6.640 eV), demonstrating that the electrons required less energy to migrate from the interior of Ru/P-NiMoO$_4$ material to the surface, thus promoting the electrochemical reaction. The partial density of states (PDOS) of individual atoms on the surface of NiMoO$_4$, Ru-NiMoO$_4$, P-NiMoO$_4$, and Ru/P-NiMoO$_4$ are used to study the electronic structural difference of NiMoO$_4$ models before and after Ru and P doping [61]. The DOS of Ru/P-NiMoO$_4$ @NF close to the Fermi level is continuous without evident gap, demonstrating the metallic property of the Ru/P-NiMoO$_4$ @NF (Fig. 5f) [62]. Fig. 5f also shows the projected DOS of the d band of the NiMoO$_4$, Ru-NiMoO$_4$, and P-NiMoO$_4$ models with the D-band centering at − 2.324, − 2.628, − 2.385 eV, respectively. According to the D-band center theory, when Ru and P elements are separately doped into the structure, the D-band center is far away from the Fermi level, thus weakening the molecular adsorption [63]. In addition, the DOS of Ru/P-NiMoO$_4$ at the Fermi level significantly increases after Ru and P co-doping, indicating that more charge carriers participate in the catalytic reaction and the catalytic performance is significantly improved. Furthermore, the increased DOS at the Fermi level enhances the electrical conductivity with fast interfacial electron-transfer kinetics. The above results demonstrate that the Ru/P doping can modulate the D-band center of catalyst, thus enhancing the adsorption of reactants and reaction intermediates, synergistically improving the activity of HER and UOR.

4. Conclusions

We demonstrated that the integrated electrode composed of Ru, P co-doped multichannel NiMoO$_4$ nanorods grown on Ni foam (denoted as Ru/P-NiMoO$_4$ @NF) exhibit bifunctional electrocatalytic activity for driving large current density toward HER and UOR. Specifically, the optimized Ru/P-NiMoO$_4$ @NF can achieve 3000 mA cm^{-2} with an ultralow working potential of 0.23 mV for HER and 1000 mA cm^{-2} with 1.46 V for UOR in alkaline seawater electrolyte. Application of Ru/P-NiMoO$_4$ @NF as both anode and cathode catalysts for OUS in the two-electrode electrolyzer only require an ultralow voltage of 1.73 V to achieve a current density of 500 mA cm^{-2} and long-term stability (up to 145 h) to keep the current density above 100 mA cm^{-2}, which outperform the state-of-the-art catalysts. The DFT calculations clarify the reasons for the enhanced HER and UOR performances, where the Ru and P dual-doping can modulate the D-band center of catalyst, thus enhancing the adsorption of reactants and reaction intermediates. Hence, this work provides a cost-effective strategy for producing green hydrogen and realizing a carbon-neutral economy and contamination-free environment.

CRediT authorship contribution statement

Lili Guo: Investigation, Data curation, Conceptualization, Formal analysis, Validation, Writing – original draft. **Jingqi Chi:** Investigation, Data curation, Conceptualization, Formal analysis, Validation, Writing – original draft. **Jiawei Zhu:** Investigation, Data curation, Conceptualization, Formal analysis. **Tong Cui:** Data curation, Conceptualization. **Jianping Lai:** Writing – review & editing, Supervision. **Lei Wang:** Supervision, Funding acquisition.

Declaration of Competing Interest

The authors declare that they have no known competing financial interests or personal relationships that could have appeared to influence the work reported in this paper.

Data availability

The data that has been used is confidential.

Appendix A. Supporting information

Supplementary data associated with this article can be found in the online version at doi:10.1016/j.apcatb.2022.121977.

References

[1] J. Chang, G. Wang, Z. Yang, B. Li, Q. Wang, R. Kuliiev, N. Orlovskaya, M. Gu, Y. Du, G. Wang, Y. Yang, Dual-doping and synergism toward high-performance seawater electrolysis, Adv. Mater. 33 (2021), e2101425, https://doi.org/10.1002/adma.202101425.

[2] H. Xue, A. Meng, H. Zhang, Y. Lin, Z. Li, C. Wang, 3D urchin like V-doped CoP in situ grown on nickel foam as bifunctional electrocatalyst for efficient overall water-splitting, Nano Res. 14 (2021) 4173–4181, https://doi.org/10.1007/s12274-021-3359-2.

[3] M.A. Ahsan, T. He, K. Eid, A.M. Abdullah, M.L. Curry, A. Du, A.R. Puente Santiago, L. Echegoyen, J.C. Noveron, Tuning the intermolecular electron transfer of low-dimensional and metal-free bcn/c60 electrocatalysts via interfacial defects for efficient hydrogen and oxygen electrochemistry, J. Am. Chem. Soc. 143 (2021) 1203–1215, https://doi.org/10.1021/jacs.0c12386.

[4] P.M. Csernica, J.R. McKone, C.R. Mulzer, W.R. Dichtel, H.D. Abruña, F.J. DiSalvo, Electrochemical hydrogen evolution at ordered Mo$_7$Ni$_7$, ACS Catal. 7 (2017) 3375–3383, https://doi.org/10.1021/acscatal.7b00344.

[5] S. Shit, S. Bolar, N.C. Murmu, T. Kuila, An account of the strategies to enhance the water splitting efficiency of noble-metal-free electrocatalysts, J. Energy Chem. 59 (2021) 160–190, https://doi.org/10.1016/j.jechem.2020.10.022.

[6] L. Wu, F. Zhang, S. Song, M. Ning, Q. Zhu, J. Zhou, G. Gao, Z. Chen, Q. Zhou, X. Xing, T. Tong, Y. Yao, J. Bao, L. Yu, S. Chen, Z. Ren, Efficient alkaline water/seawater hydrogen evolution by a nanorod-nanoparticle-structured Ni-MoN catalyst with fast water-dissociation kinetics, Adv. Mater. 34 (2022), e2201774, https://doi.org/10.1002/adma.202201774.

[7] L. Yu, Q. Zhu, S. Song, B. McElhenny, D. Wang, C. Wu, Z. Qin, J. Bao, Y. Yu, S. Chen, Z. Ren, Non-noble metal-nitride based electrocatalysts for high-performance alkaline seawater electrolysis, Nat. Commun. 10 (2019) 5106, https://doi.org/10.1038/s41467-019-13092-7.

[8] Q. Zhao, Y. Wang, W.-H. Lai, F. Xiao, Y. Lyu, C. Liao, M. Shao, Approaching a high-rate and sustainable production of hydrogen peroxide: oxygen reduction on Co-N-C single-atom electrocatalysts in simulated seawater, Energy Environ. Sci. 14 (2021) 5444–5456, https://doi.org/10.1039/d1ee00878a.

[9] H.J. Song, H. Yoon, B. Ju, D.-Y. Lee, D.-W. Kim, Electrocatalytic selective oxygen evolution of carbon-coated Na$_2$Co$_{1-x}$Fe$_x$P$_2$O$_7$ nanoparticles for alkaline seawater electrolysis, ACS Catal. 10 (2020) 702–709, https://doi.org/10.1021/acscatal.9b04231.

[10] Y. Zhao, B. Jin, Y. Zheng, H. Jin, Y. Jiao, S.-Z. Qiao, Charge state manipulation of cobalt selenide catalyst for overall seawater electrolysis, Adv. Energy Mater. 8 (2018) 1801926, https://doi.org/10.1002/aenm.201801926.

[11] N.K. Oh, C. Kim, J. Lee, O. Kwon, Y. Choi, G.Y. Jung, H.Y. Lim, S.K. Kwak, G. Kim, H. Park, In-situ local phase-transitioned MoSe$_2$ in La$_{0.5}$Sr$_{0.5}$CoO$_{3-\delta}$ heterostructure and stable overall water electrolysis over 1000 h, Nat. Commun. 10 (2019) 1723, https://doi.org/10.1038/s41467-019-09339-y.

[12] M. Ning, F. Zhang, L. Wu, X. Xing, D. Wang, S. Song, Q. Zhou, L. Yu, J. Bao, S. Chen, Z. Ren, Boosting efficient alkaline fresh water and seawater electrolysis via electrochemical reconstruction, Energy Environ. Sci. (2022), https://doi.org/10.1039/D2EE01094A.

[13] S. Dresp, F. Dionigi, M. Klingenhof, P. Strasser, Direct electrolytic splitting of seawater: opportunities and challenges, ACS Energy Lett. 4 (2019) 933–942, https://doi.org/10.1021/acsenergylett.9b00220.

[14] S. Riyajuddin, K. Azmi, M. Pahuja, S. Kumar, T. Maruyama, C. Bera, K. Ghosh, Super-hydrophilic hierarchical Ni-foam-graphene-carbon nanotubes-Ni$_2$P-CuP$_2$ nano-architecture as efficient electrocatalyst for overall water splitting, ACS Nano 15 (2021) 5586–5599, https://doi.org/10.1021/acsnano.1c00647.

[15] Z. Liu, F. Guo, L. Han, J. Xiao, X. Zeng, C. Zhang, P. Dong, M. Li, Y. Zhang, Manganese oxide/iron carbide encapsulated in nitrogen and boron codoped carbon nanowire networks as accelerated alkaline hydrogen evolution and oxygen reduction bifunctional electrocatalysts, ACS Appl. Mater. Interfaces 14 (2022) 13280–13294, https://doi.org/10.1021/acsami.1c23731.

[16] F.S. Hegner, F.A. Garcés-Pineda, J. González-Cobos, B. Rodríguez-García, M. Torréns, E. Palomares, N. López, J.-R. Galán-Mascarós, Understanding the catalytic selectivity of cobalt hexacyanoferrate toward oxygen evolution in seawater electrolysis, ACS Catal. 11 (2021) 13140–13148, https://doi.org/10.1021/acscatal.1c03502.

[17] S. Dresp, T. Ngo Thanh, M. Klingenhof, S. Brückner, P. Hauke, P. Strasser, Efficient direct seawater electrolysers using selective alkaline NiFe-LDH as OER catalyst in asymmetric electrolyte feeds, Energy Environ. Sci. 13 (2020) 1725–1729, https://doi.org/10.1039/d0ee01125h.

[18] Z. Yan, H. Sun, X. Chen, H. Liu, Y. Zhao, H. Li, W. Xie, F. Cheng, J. Chen, Anion insertion enhanced electrodeposition of robust metal hydroxide/oxide electrodes for oxygen evolution, Nat. Commun. 9 (2018) 2373, https://doi.org/10.1038/s41467-018-04788-3.

[19] L. Peng, N. Yang, Y. Yang, Q. Wang, X. Xie, D. Sun-Waterhouse, L. Shang, T. Zhang, G.I.N. Waterhouse, Atomic cation-vacancy engineering of NiFe-layered double hydroxides for improved activity and stability towards the oxygen evolution reaction, Angew. Chem. Int. Ed. 60 (2021) 24612–24619, https://doi.org/10.1002/anie.202109938.

[20] S. Khatun, P. Roy, Cobalt chromium vanadium layered triple hydroxides as an efficient oxygen electrocatalyst for alkaline seawater splitting, Chem. Commun. 58 (2022) 1104–1107, https://doi.org/10.1039/d1cc05745f.

[21] Tu Haq, M. Pasha, Y. Tong, S.A. Mansour, Y. Haik, Au nanocluster coupling with Gd-Co₂B nanoflakes embedded in reduced TiO₂ nanosheets: seawater electrolysis at low cell voltage with high selectivity and corrosion resistance, Appl. Catal. B Environ. 301 (2022) 120836, https://doi.org/10.1016/j.apcatb.2021.120836.

[22] J. Zhang, T. Wang, P. Liu, Z. Liao, S. Liu, X. Zhuang, M. Chen, E. Zschech, X. Feng, Efficient hydrogen production on MoNi₄ electrocatalysts with fast water dissociation kinetics, Nat. Commun. 8 (2017) 15437, https://doi.org/10.1038/ncomms15437.

[23] A.M. El-Sawy, I.M. Mosa, D. Su, C.J. Guild, S. Khalid, R. Joesten, J.F. Rusling, S. L. Suib, Controlling the active sites of sulfur-doped carbon nanotube-graphene nanolobes for highly efficient oxygen evolution and reduction catalysis, Adv. Energy Mater. 6 (2016), https://doi.org/10.1002/aenm.201670028.

[24] V.K. Singh, U. Gupta, B. Mukherjee, S. Chattopadhyay, S. Das, MoS₂ nanosheets on MoNi₄/MoO₂ nanorods for hydrogen evolution, ACS Appl. Nano Mater. 4 (2021) 886–896, https://doi.org/10.1021/acsanm.0c03296.

[25] C. Chen, S. He, K. Dastafkan, Z. Zou, Q. Wang, C. Zhao, Sea urchin-like NiMoO₄ nanorod arrays as highly efficient bifunctional catalysts for electrocatalytic/photovoltage-driven urea electrolysis, Chin. J. Catal. 43 (2022) 1267–1276, https://doi.org/10.1016/s1872-2067(21)63962-1.

[26] H. Jiang, M. Sun, S. Wu, B. Huang, C.S. Lee, W. Zhang, Oxygen-incorporated NiMoP nanotube arrays as efficient bifunctional electrocatalysts for urea-assisted energy-saving hydrogen production in alkaline electrolyte, Adv. Funct. Mater. 31 (2021) 2104951, https://doi.org/10.1002/adfm.202104951.

[27] Q. Zhang, F.M.D. Kazim, S. Ma, K. Qu, M. Li, Y. Wang, H. Hu, W. Cai, Z. Yang, Nitrogen dopants in nickel nanoparticles embedded carbon nanotubes promote overall urea oxidation, Appl. Catal. B Environ. 280 (2021) 119436, https://doi.org/10.1016/j.apcatb.2020.119436.

[28] J. Wang, Y. Sun, Y. Qi, C. Wang, Vanadium-doping and interface engineering for synergistically enhanced electrochemical overall water splitting and urea electrolysis, ACS Appl. Mater. Interfaces 13 (2021) 57392–57402, https://doi.org/10.1021/acsami.1c18593.

[29] L. Zhang, L. Wang, H. Lin, Y. Liu, J. Ye, Y. Wen, A. Chen, L. Wang, F. Ni, Z. Zhou, S. Sun, Y. Li, B. Zhang, H. Peng, A. Lattice-Oxygen-Involved, Reaction pathway to boost urea oxidation, Angew. Chem. Int. Ed. 58 (2019) 16820–16825, https://doi.org/10.1002/anie.201909832.

[30] C. Li, H. Jang, S. Liu, M.G. Kim, L. Hou, X. Liu, J. Cho, P and Mo dual doped Ru ultrasmall nanoclusters embedded in P-doped porous carbon toward efficient hydrogen evolution reaction, Adv. Energy Mater. (2022) 2200029, https://doi.org/10.1002/aenm.202200029.

[31] S.A. Patil, S. Cho, Y. Jo, N.K. Shrestha, H. Kim, H. Im, Bimetallic Ni-Co@hexacyano nano-frameworks anchored on carbon nanotubes for highly efficient overall water splitting and urea decontamination, Chem. Eng. J. 426 (2021) 130773, https://doi.org/10.1016/j.cej.2021.130773.

[32] W. Sun, J. Li, W. Gao, L. Kang, F. Lei, J. Xie, Recent advances in the pre-oxidation process in electrocatalytic urea oxidation reactions, Chem. Commun. 58 (2022) 2430–2442, https://doi.org/10.1039/d1cc06290e.

[33] N. Chen, Y.-X. Du, G. Zhang, W.-T. Lu, F.-F. Cao, Amorphous nickel sulfoselenide for efficient electrochemical urea-assisted hydrogen production in alkaline media, Nano Energy 81 (2021) 105605, https://doi.org/10.1016/j.nanoen.2020.105605.

[34] D. Zhu, H. Zhang, J. Miao, F. Hu, L. Wang, Y. Tang, M. Qiao, C. Guo, Strategies for designing more efficient electrocatalysts towards the urea oxidation reaction, J. Mater. Chem. A 10 (2022) 3296–3313, https://doi.org/10.1039/d1ta09989b.

[35] Q. Xu, T. Yu, J. Chen, G. Qian, H. Song, L. Luo, Y. Chen, T. Liu, Y. Wang, S. Yin, Coupling interface constructions of FeNi₃-MoO₂ heterostructures for efficient urea oxidation and hydrogen evolution reaction, ACS Appl. Mater. Interfaces 13 (2021) 16355–16363, https://doi.org/10.1021/acsami.1c01188.

[36] C. Xiao, S. Li, X. Zhang, D.R. MacFarlane, MnO₂/MnCo₂O₄/Ni heterostructure with quadruple hierarchy: a bifunctional electrode architecture for overall urea oxidation, J. Mater. Chem. A 5 (2017) 7825–7832, https://doi.org/10.1039/c7ta00980a.

[37] M. Safeer, N.K. C, R. Alex, A. Jana, N.S. Datta, John, Remarkable COx tolerance of Ni³⁺ active species in a Ni₂O₃ catalyst for sustained electrochemical urea oxidation, J. Mater. Chem. A 10 (2022) 4209–4221, https://doi.org/10.1039/d1ta05753g.

[38] W. Zhu, Z. Yue, W. Zhang, N. Hu, Z. Luo, M. Ren, Z. Xu, Z. Wei, Y. Suo, J. Wang, Wet-chemistry topotactic synthesis of bimetallic iron–nickel sulfide nanoarrays: an advanced and versatile catalyst for energy efficient overall water and urea electrolysis, J. Mater. Chem. A 6 (2018) 4346–4353, https://doi.org/10.1039/c7ta10584c.

[39] Z. Gao, Y. Wang, L. Xu, Q. Tao, X. Wang, Z. Zhou, Y. Luo, J. Yu, Y. Huang, Optimizing local charge distribution of metal nodes in bimetallic metal–organic frameworks for efficient urea oxidation reaction, Chem. Eng. J. 433 (2022), 133515, https://doi.org/10.1016/j.cej.2021.133515.

[40] G. Kresse, J. Furthmüller, Efficiency of ab-initio total energy calculations for metals and semiconductors using a plane-wave basis set, Comput. Mater. Sci. 6 (1996) 15–50, https://doi.org/10.1016/0927-0256(96)00008-0.

[41] P.E. Blöchl, Projector augmented-wave method, Phys. Rev. B 50 (1994) 17953–17979, https://doi.org/10.1103/physrevb.50.17953.

[42] J.P. Perdew, J.A. Chevary, S.H. Vosko, K.A. Jackson, M.R. Pederson, D.J. Singh, C. Fiolhais, Atoms, molecules, solids, and surfaces: applications of the generalized gradient approximation for exchange and correlation, Phys. Rev. B 46 (1992) 6671–6687, https://doi.org/10.1103/physrevb.46.6671.

[43] S. Grimme, J. Antony, S. Ehrlich, H. Krieg, A consistent and accurate ab initio parametrization of density functional dispersion correction (DFT-D) for the 94 elements H-Pu, J. Chem. Phys. 132 (2010), 154104, https://doi.org/10.1063/1.3382344.

[44] Y. Xu, S. Yu, T. Ren, S. Liu, Z. Wang, X. Li, L. Wang, H. Wang, Hydrophilic/aerophobic hydrogen-evolving electrode: NiRu-based metal-organic framework nanosheets in situ grown on conductive substrates, ACS Appl. Mater. Interfaces 12 (2020) 34728–34735, https://doi.org/10.1021/acsami.0c03333.

[45] Y.-Y. Chen, Y. Zhang, X. Zhang, T. Tang, H. Luo, S. Niu, Z.-H. Dai, L.-J. Wan, J.-S. Hu, Self-templated fabrication of MoNi₄/MoO₃₋ₓ nanorod arrays with dual active components for highly efficient hydrogen evolution, Adv. Mater. 29 (2017) 1703311, https://doi.org/10.1002/adma.201703311.

[46] W. Du, Y. Shi, W. Zhou, Y. Yu, B. Zhang, Unveiling the in situ dissolution and polymerization of Mo in Ni₄Mo alloy for promoting the hydrogen evolution reaction, Angew. Chem. Int. Ed. 60 (2021) 7051–7055, https://doi.org/10.1002/anie.202015723.

[47] C. Andronescu, S. Barwe, E. Ventosa, J. Masa, E. Vasile, B. Konkena, S. Möller, W. Schuhmann, Powder catalyst fixation for post-electrolysis structural characterization of nife layered double hydroxide based oxygen evolution reaction electrocatalysts, Angew. Chem. Int. Ed. 56 (2017) 11258–11262, https://doi.org/10.1002/anie.201705385.

[48] G. Zhang, Y. Li, X. Xiao, Y. Shan, Y. Bai, H.G. Xue, H. Pang, Z. Tian, Q. Xu, In situ anchoring polymetallic phosphide nanoparticles within porous prussian blue analogue nanocages for boosting oxygen evolution catalysis, Nano Lett. 21 (2021) 3016–3025, https://doi.org/10.1021/acs.nanolett.1c00179.

[49] Q. Zhou, Q. Hao, Y. Li, J. Yu, C. Xu, H. Liu, S. Yan, Free-standing trimodal porous NiZn intermetallic and Ni heterojunction as highly efficient hydrogen evolution electrocatalyst in the alkaline electrolyte, Nano Energy 89 (2021) 106402, https://doi.org/10.1016/j.nanoen.2021.106402.

[50] Z. Zhang, X. Liu, D. Wang, H. Wan, Y. Zhang, G. Chen, N. Zhang, R. Ma, Ruthenium composited NiCo₂O₄ spinel nanocones with oxygen vacancies as a high-efficient bifunctional catalyst for overall water splitting, Chem. Eng. J. 446 (2022), 137037, https://doi.org/10.1016/j.cej.2022.137037.

[51] C. Jin, P. Zhai, Y. Wei, Q. Chen, X. Wang, W. Yang, J. Xiao, Q. He, Q. Liu, Y. Gong, Ni(OH)₂ templated synthesis of ultrathin Ni₃S₂ nanosheets as bifunctional electrocatalyst for overall water splitting, Small 17 (2021), e2102097, https://doi.org/10.1002/smll.202102097.

[52] L. Wu, L. Yu, B. McElhenny, X. Xing, D. Luo, F. Zhang, J. Bao, S. Chen, Z. Ren, Rational design of core-shell-structured CoP@FeOOH for efficient seawater electrolysis, Appl. Catal. B Environ. 294 (2021) 120256, https://doi.org/10.1016/j.apcatb.2021.120256.

[53] Z. Zhang, Y. Zhang, C. Feng, H. Wu, Y. Ding, H. Mei, P doped NiCoZn LDH growth on nickel foam as an highly efficient bifunctional electrocatalyst for overall urea-water electrolysis, Int. J. Hydrog. Energy 46 (2021) 25321–25331, https://doi.org/10.1016/j.ijhydene.2021.05.076.

[54] J. Yu, Y. Guo, S. She, S. Miao, M. Ni, W. Zhou, M. Liu, Z. Shao, Bigger is surprisingly better: agglomerates of larger RuP nanoparticles outperform benchmark Pt nanocatalysts for the hydrogen evolution reaction, Adv. Mater. 30 (2018) 1800047, https://doi.org/10.1002/adma.201800047.

[55] K. Yang, P. Xu, Z. Lin, Y. Yang, P. Jiang, C. Wang, S. Liu, S. Gong, L. Hu, Q. Chen, Ultrasmall Ru/Cu-doped RuO₂ complex embedded in amorphous carbon skeleton as highly active bifunctional electrocatalysts for overall water splitting, Small 14 (2018) 1803009, https://doi.org/10.1002/smll.201803009.

[56] Y. Ding, Y. Peng, S. Chen, Z. Li, X. Zhang, P. Falaras, L. Hu, A competitive coordination strategy to synthesize Co₃O₄/carbon flower-like structures for high-performance asymmetric supercapacitors, Appl. Surf. Sci. 495 (2019) 143502, https://doi.org/10.1016/j.apsusc.2019.07.244.

[57] M. Qu, Y. Jiang, M. Yang, S. Liu, Q. Guo, W. Shen, M. Li, R. He, Regulating electron density of NiFe-P nanosheets electrocatalysts by a trifle of Ru for high-efficient overall water splitting, Appl. Catal. B Environ. 263 (2020), 118324, https://doi.org/10.1016/j.apcatb.2019.118324.

[58] L. Wu, L. Yu, F. Zhang, B. McElhenny, D. Luo, A. Karim, S. Chen, Z. Ren, Heterogeneous bimetallic phosphide Ni₂P-Fe₂P as an efficient bifunctional catalyst for water/seawater splitting, Adv. Funct. Mater. 31 (2020) 2006484, https://doi.org/10.1002/adfm.202006484.

[59] M. Yao, B. Wang, B. Sun, L. Luo, Y. Chen, J. Wang, N. Wang, S. Komarneni, X. Niu, W. Hu, Rational design of self-supported Cu@WC core-shell mesoporous nanowires

for pH-universal hydrogen evolution reaction, Appl. Catal. B Environ. 280 (2021), 119451, https://doi.org/10.1016/j.apcatb.2020.119451.

[60] Y. Liu, J. Zhang, Y. Li, Q. Qian, Z. Li, G. Zhang, Realizing the synergy of interface engineering and chemical substitution for Ni$_3$N enables its bifunctionality toward hydrazine oxidation assisted energy-saving hydrogen production, Adv. Funct. Mater. 31 (2021) 2103673, https://doi.org/10.1002/adfm.202103673.

[61] B. Zhang, C. Li, J. Hu, D. Peng, K. Huang, J. Wu, Z. Chen, Y. Huang, Cobalt tungsten phosphide with tunable W-doping as highly efficient electrocatalysts for hydrogen evolution reaction, Nano Res. 14 (2021) 4073–4078, https://doi.org/10.1007/s12274-021-3342-y.

[62] M.S. Kim, D.T. Tran, T.H. Nguyen, V.A. Dinh, N.H. Kim, J.H. Lee, Ni single atoms and Ni phosphate clusters synergistically triggered surface-functionalized MoS$_2$ nanosheets for high-performance freshwater and seawater electrolysis, Energy Environ. Mater. (2022), https://doi.org/10.1002/eem2.12366.

[63] L. Zhang, Y. Zhu, Z. Nie, Z. Li, Y. Ye, L. Li, J. Hong, Z. Bi, Y. Zhou, G. Hu, Co/MoC nanoparticles embedded in carbon nanoboxes as robust trifunctional electrocatalysts for a Zn-air battery and water electrocatalysis, ACS Nano 15 (2021) 13399–13414, https://doi.org/10.1021/acsnano.1c03766.